

Flame-synthesized LaCoO₃-supported Pd

1. Structure, thermal stability and reducibility

Gian Luca Chiarello^a, Jan-Dierk Grunwaldt^b, Davide Ferri^b, Frank Krumeich^b, Cesare Oliva^a,
Lucio Forni^{a,*}, Alfons Baiker^b

^a Dipartimento di Chimica Fisica ed Elettrochimica, Università degli Studi di Milano, v. C. Golgi 19, I-20133 Milano, Italy

^b Institute for Chemical and Bioengineering, Department of Chemistry and Applied Biosciences, ETH Zurich, Hönggerberg, 8093 Zurich, Switzerland

Received 18 July 2007; revised 25 September 2007; accepted 2 October 2007

Abstract

Nanosized LaCoO₃ (LCO) and 0.5 wt% Pd/LaCoO₃ (PdLCO) were synthesized in a single step by flame-spray pyrolysis (FP) and characterized by N₂ adsorption–desorption at 77 K (BET), electron microscopy (HRTEM, STEM-EDXS), *in situ* XRD, *in situ* fluorescence XANES and EXAFS (around the Pd K-edge), EPR, and H₂ TGA-TPR. The stability of the perovskite structure under different treatments and the location of Pd were addressed by calcination at 600 and 800 °C and successive reduction in 10% H₂/He to 300 and 600 °C. The as-prepared PdLCO exhibited a high surface area (ca. 100 m²/g). Palladium appeared to be finely dispersed on the FP material and was partially incorporated in the perovskite lattice. Calcination at 800 °C caused sintering and substantial incorporation of Pd at the B-site of the ABO₃ framework. EXAFS revealed that the Pd–O distance was shorter than in PdO and further decreased with increasing calcination temperature, simultaneously with the appearance of a Pd–La contribution. The reduction process involved both Pd and Co. In the 100–300 °C range, the reduction of Co³⁺ to Co²⁺ (from LaCoO₃ to La₂Co₂O₅) and the segregation of Pd in the form of metal particles occurred. The reduction of Co was already reversible at 120 °C, and the perovskite structure was restored after exposure to oxygen. In contrast, Pd remained in the metallic state. Therefore, the final structure of PdLCO after mild reoxidation consisted of Pd and Co particles supported on LaCoO₃. In contrast, reduction at 600 °C led to the formation of a Pd–Co alloy. The composition of PdLCO reduced at different temperatures is likely to strongly influence the catalytic processes involved in combustion exhaust after treatment.

© 2007 Elsevier Inc. All rights reserved.

Keywords: Flame-spray pyrolysis; Pd/LaCoO₃ perovskite; *In situ* fluorescence XANES; EXAFS; *In situ* XRD-QMS-TGA; Exhaust gas catalysis

1. Introduction

Pd-based materials are well known highly active catalysts for a wide range of heterogeneous reactions, from fine chemical synthesis [1] to partial or full oxidation reactions [2–4]. The catalytic removal of pollutants from the exhaust of internal combustion engines (e.g., as part of a three-way catalyst) is perhaps one of their most important applications [5]. Among these, Pd supported on perovskite-like mixed oxides are promising materials in which the chemical properties of the noble metal are coupled with those of the support [6–16]. These materials,

for example, exhibit higher selectivity to N₂ compared with the traditional Pt or Pd supported on Al₂O₃ or SiO₂, when used as catalysts for the selective reduction of NO by H₂ (H₂-SCR) under lean-burn conditions [9–12]. Indeed, along with the reaction occurring on the noble metal surface, the formation of different active nitrogen-containing species adsorbed on the perovskite surface has been observed. These species are reduced to N₂ by hydrogen spillover from the noble metal [13]. An important and successful example of the precious metal–perovskite combination is LaFe_{0.95}Pd_{0.05}O₃ [17,18]. The advantage of such perovskite systems is that Pd can be reversibly incorporated into the lattice on oxidation and segregated out as small particles. This behavior represents a sort of self-regeneration mechanism, which confers a superior resistance to the catalyst by preventing sintering of Pd particles. This material satisfies the stringent

* Corresponding author. Fax: +39 02 50314300.
E-mail address: lucio.forni@unimi.it (L. Forni).

vehicle ultra-low-emission standards and has been commercialized for automotive exhaust aftertreatment in Japan [19]. LaCoO₃ is particularly attractive, because it is one of the most reducible ABO₃-type perovskites [20] and displays a rich phase behavior under reducing conditions [21,22], which can be significantly influenced on addition of a noble metal such as Pd, Pt, Rh, or Cu [11,22,23].

The usual synthetic route to perovskite-supported noble metals is based on conventional wet chemistry procedures, involving the preparation of the oxidic support, followed by loading of the noble metal(s) by impregnation from aqueous solution. These routes require several batch steps and are experimentally tedious. Moreover, the resultant crystal phase before catalysis is often not composed solely of a perovskite-supported noble metal but rather is a mixture of metal oxides, possibly including a perovskite.

Flame-spray pyrolysis (FP) [24,25] is an efficient and attractive single-step method suitable for continuous large-scale production of catalytic materials in the form of nanoparticle powders having high BET specific surface areas (SSAs) [26–32]. Several studies have investigated the preparation of supported metals [28,32–37] and alloys [36,38–40]. Only recently it has been shown that perovskites also can be prepared by this method [41–43]. Therefore, the aim of the present work was to prepare a 0.5 wt% Pd/LaCoO₃ (PdLCO) catalyst by FP and to determine the structure of Pd and of the perovskite support through the detailed characterization of the flame-made PdLCO material after preparation, during calcination to 800 °C, and during successive reduction to 600 °C and compare it with the Pd-free LaCoO₃ (LCO). This material is a potential candidate for the low-temperature H₂-SCR of NO in the presence of excess oxygen [11,44]. In particular, changes in the crystal phase were monitored using *in situ* X-ray diffraction (XRD) coupled with quadrupolar mass spectrometric–thermogravimetric analysis (QMS–TGA). The changes in the oxidation state of palladium were monitored in the fluorescence mode by *in situ* X-ray absorption near-edge structure (XANES) and extended X-ray absorption fine-structure (EXAFS) at the Pd K-edge. Finally, additional important information was gained from the comparison of the high-resolution electron microscopy (HRTEM) and STEM-EDXS patterns of PdLCO and of a 0.5 wt% Pd/LaCoO₃ sample (imp-PdLCO) obtained by impregnation of LCO with a Pd salt.

All of the information collected here represents a solid basis for the catalytic application of this material, particularly for the interpretation of the catalytic behavior of this system in H₂-SCR under lean-burn conditions, which will be the target of a future study [44].

2. Experimental

2.1. Catalyst preparation

La(CH₃COO)₃·xH₂O (Aldrich, purity >99.9%, H₂O 7.5 wt%, determined by TGA) and Co(CH₃COO)₂·4H₂O (Merck, purum) were dissolved in a mixture of propionic acid, *n*-propanol, and water (5:4:1 vol%) under vigorous stirring

at 60 °C, to obtain a 1:1 metal–ion ratio and a 0.15 M overall metal concentration (sample LCO). The desired amount of Pd(CH₃COO)₂ (Fluka, purum) was added when preparing the Pd-containing sample (PdLCO).

The liquid solution was fed at a rate of 4 mL/min by a microannular gear pump (HNP Mikrosysteme model mzzr 2905) at the center of a vertical nozzle, together with 5 L/min of O₂ (1 bar pressure drop across the nozzle). The obtained spray was ignited, and the flame was supported by a premixed methane/oxygen (1.0 L/min O₂ and 0.5 L/min CH₄) annular flame (12 mm diameter, 0.15 mm thick) surrounding the nozzle. The powder thus produced was collected on a glass fiber filter (Whatman GF/D, 25.7 cm diameter) connected to a vacuum pump (Busch Seco SV 1040C).

A 0.5 wt% Pd/LaCoO₃ (impPdLCO) was also prepared by incipient wetness impregnation of a portion of the FP-made perovskite (LCO) with a solution of (NH₄)₂PdCl₄ (Fluka, puriss.). In detail, the LCO was precalcined at 800 °C and then dispersed in an aqueous solution containing the desired amount of Pd, so as to have a final 0.5 wt% of noble metal on the support. The suspension was slowly stirred for 6 h and then evaporated in a rotavapor. The powder thus obtained was then dried overnight at 90 °C and finally calcined in flowing 10% O₂/He at 500 °C for 2 h before use.

2.2. Characterization methods

The BET SSA was measured by N₂ adsorption/desorption at 77 K on a Micromeritics ASAP 2010 apparatus, after outgassing *in vacuo* at 300 °C for at least 6 h. For HRTEM and STEM, the material was dispersed in ethanol and deposited onto a perforated carbon foil, supported on a copper grid. The analysis was done on a Tecnai F30 microscope (FEI, Eindhoven; field emission cathode) operated at 300 kV. STEM images, obtained with a high-angle annular dark field (HAADF) detector, reveal metal particles with bright contrast (Z contrast). Energy dispersive X-ray spectroscopy (EDXS) was applied using an EDAX system attached to the Tecnai F30 microscope. Electron paramagnetic resonance (EPR) and ferromagnetic resonance (FMR) spectra were recorded at 298 and 77 K using a Bruker Elexsys spectrometer at the working frequency of 9.4 GHz. *In situ* XRD analysis was performed at the bending magnet beamline B2 at HASYLAB, Hamburg, Germany. The storage ring typically operates at 4.45 GeV with a ring current of 80–120 mA. The powder diffractograms were obtained above the Pd K-edge at $\lambda = 0.4720 \text{ \AA}$ using a Si(111) double crystal as a monochromator. The 2θ axis of the XRD patterns was converted to the more common laboratory wavelength of the CuK α radiation ($\lambda = 1.5406 \text{ \AA}$) for a better comparison. The obtained patterns were compared with the Inorganic Crystal Structure Database (ICSD) data for phase identification. The average crystal diameter was calculated by fitting with a Gauss function the profile of the reflection at $2\theta = 47.7^\circ$ (selected as the most intense single peak) to calculate the integral peak width β (rad) (i.e., the peak area/peak intensity ratio) and by applying Scherrer's equation:

$$D_{\text{XRD}} \text{ (nm)} = \lambda \text{ (nm)} / (\beta \cos \theta).$$

XANES and EXAFS data were collected using a Si(111) double-crystal monochromator in the step scanning mode at the Norwegian–Swiss beamline (SNBL, BM01B) of the European Synchrotron Radiation Facility (ESRF, Grenoble, France). The spectra were obtained in transmission and fluorescence modes at room temperature using a specially designed *in situ* cell [45]. The spectra were collected around the Pd K-edge (24.350 keV). Because of the low Pd content and of the strong absorbance of the perovskite matrix, the transmitted X-ray beam was rather weak, leading to a low signal-to-noise ratio, so that only the fluorescence mode was successfully used to record spectra. The fluorescence signals from the 13 detector elements (13 element Ge detector, Canberra) were directly preamplified and then fed into the XIA digital pulse processing electronics (DXP 2X). The PdK α fluorescence regions were selected and calibrated on the basis of a full spectrum for each channel, collected before the measured scans. The resulting 13 SCA data were added up manually after each measurement, with the spectra background-corrected and normalized using WINXAS 3.1 software [46]. Data fitting was performed in the *R* space on the Fourier-transformed k^3 -weighted EXAFS functions (Fourier transform in the range of 3.5–14 Å; $S_0^2 = 0.7$). Theoretical scattering amplitudes and phase shifts of the Pd–Pd and Pd–O shells (first shell only) were calculated using the FEFF code [47]. In both *in situ* XRD and EXAFS experiments, the powder was pelletized, crushed, and sieved to 50–100 μm . The reaction mixtures for *in situ* oxidation and reduction were 21% O₂/He and 5% H₂/He.

2.3. H₂-TGA-TPR experiments

Thermogravimetric analysis during reduction with H₂ (TGA-TPR) of LCO and PdLCO was performed in a Netzsch STA 409 thermal analyzer [48] under the following operating conditions: 50 mL/min of 10% H₂/He and a temperature ramp of 5 °C/min up to 700 °C. The outlet of the thermal analyzer was connected to an Omnistar Pfeiffer Vacuum GSD 301 O₂ quadrupole mass spectrometer (QMS) through a heated (150 °C) stainless steel capillary tube. Before the TPR experiments, the as-prepared powder was treated in the same TGA apparatus in flowing 20% O₂/He, while heating at 5 °C/min from room temperature up to 800 °C.

3. Results and discussion

3.1. Calcination of PdLCO at 800 °C

The materials prepared by FP demonstrated an SSA of ca. 106 m²/g. According to the XRD pattern (Fig. 1), the as-prepared powder had a perovskite-like crystal phase. No features could be attributed to specific Pd-containing particles in PdLCO.

The HRTEM image showed microaggregations of single-crystal nanospheres, 4 to 10 nm in diameter (Fig. 2). The high crystallinity and size homogeneity were also seen on electron diffraction (ED) analysis (inset of Fig. 2). Indeed, the ED pattern consisted of well-defined rings, confirming the high crystallinity of the sample detected by HRTEM.

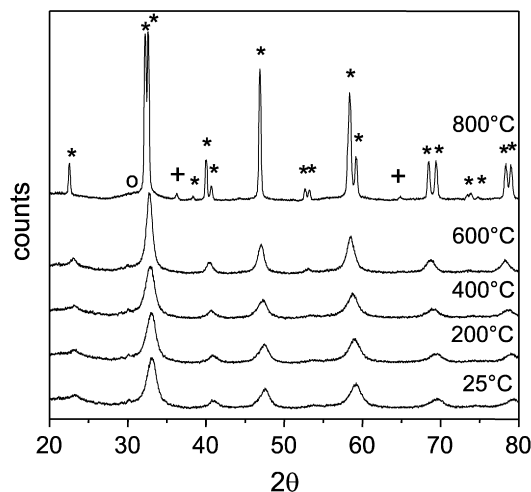


Fig. 1. *In situ* XRD of PdLCO during calcination in 21% O₂/He at the indicated temperatures: (*) LaCoO₃; (+) Co₃O₄; (o) La₂CoO₄ phases.

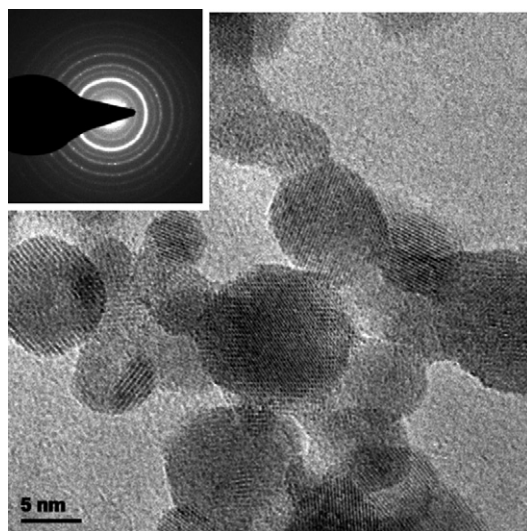


Fig. 2. HRTEM image and ED ring pattern (inset) of as-prepared FP-made PdLCO.

The as-prepared material was stable up to 400 °C under oxidizing conditions; sintering occurred at higher temperatures. The *in situ* XRD measurements during calcination up to 800 °C (Fig. 1) showed an increase of peak intensity only at 600 °C. At this temperature, the SSA decreased to 20 m²/g. After calcination at 800 °C, the reflections of the perovskite became narrower and more intense, and the SSA decreased even further, down to 8 m²/g. The crystal sizes calculated by applying Scherrer's formula were 5.3 nm for the sample calcined up to 400 °C, 8.1 nm for the sample calcined at 600 °C, and 35.6 nm for the sample calcined at 800 °C. In the latter case, a reflection appeared at $2\theta = 36.9^\circ$, attributed to a segregated Co₃O₄ phase. Such a segregation is strictly correlated with the presence of Pd. Indeed, no Co₃O₄ formation was observed on FP-LCO after calcination at 800 °C for 3 h (see Fig. 7 of [44]). On the other hand, a similar phenomenon was recently observed with flame-made La_{0.9}Ce_{0.1}CoO₃ [49], where the formation of the Co₃O₄ phase occurred during the calcination above 600 °C, after seg-

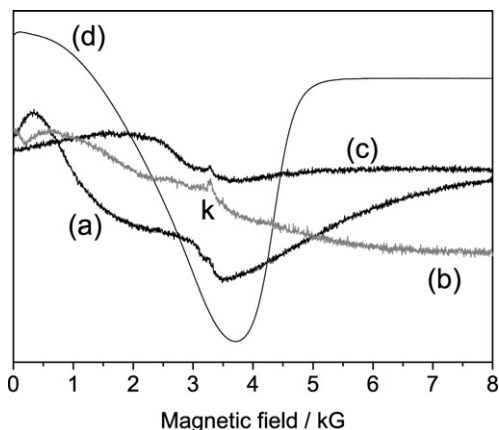


Fig. 3. EPR spectra at 298 K (a, c and d) and at 77 K (b) of PdLCO: (a) as prepared, (b) calcined at 600 °C, (c) calcined at 800 °C, (d) calcined at 800 °C and reduced at 600 °C. The bump *k* is due to the instrument cavity and not to the sample. The intensity of traces (a, b and c) was multiplied by a factor 10.

regation of a CeO₂ phase. In the present case, the presence of Pd likely induces an excess of B-site cations, thus provoking the segregation of Co as Co₃O₄. The peaks of this phase are not visible in the pattern of PdLCO calcined at 600 °C, probably because of the very small size of the crystals. The sintering occurring after calcination at 800 °C produced larger crystals, detectable by XRD.

Information on the oxidation state of Pd can be obtained by EPR, because the paramagnetic 4d⁷ and 4d⁹ electron configuration of Pd³⁺ and Pd⁺ can be distinguished from the diamagnetic 4d⁸ and 4d⁶ configuration of Pd²⁺ and Pd⁴⁺. The formation of Pd³⁺ ions has been observed on oxidation of palladium-containing catalysts at sufficiently high temperature [50–53]. In particular, well-characterized EPR spectra of Pd³⁺ species in the $g \approx 2$ spectral region have been reported with Pd-doped yttria oxidized at 600 °C [53]. In contrast, such a spectrum was not observed either in as-prepared PdLCO or after calcination at 600 and 800 °C. This indicates that only Pd²⁺ and/or Pd⁴⁺ were/was present in PdLCO (Fig. 3). The absence of Pd³⁺ is a major difference with respect to LaFePdO_x [18], in which XPS showed that Pd was predominately in this oxidation state in the calcined and reoxidized material.

In the as-prepared material, a weak ferromagnetic resonance spectrum was recorded (Fig. 3a) that disappeared after sample calcination at 800 °C; therefore, this signal could be attributed to the nanosized structure of these particles [54]. The residual low-intensity broad EPR signal observed with the sample calcined at 800 °C (Fig. 3c) is attributable to the segregated Co₃O₄ phase [51].

XANES and EXAFS at the Pd K-edge measurements of PdLCO as-prepared, precalcined at 600 °C, and precalcined at 800 °C are reported in Fig. 4. In all of these samples, XANES spectra (Fig. 4a) exhibits a typical white line at 24.37 keV, indicating that the Pd is oxidized. This result is supported by the Fourier-transformed EXAFS spectra (Fig. 4b) and data fitting (Table 1), which show a clear contribution at 1.7 Å (scale not corrected for the phase shift) due to the oxygen first-neighbor shell, thus demonstrating that Pd is surrounded by oxygen. Note

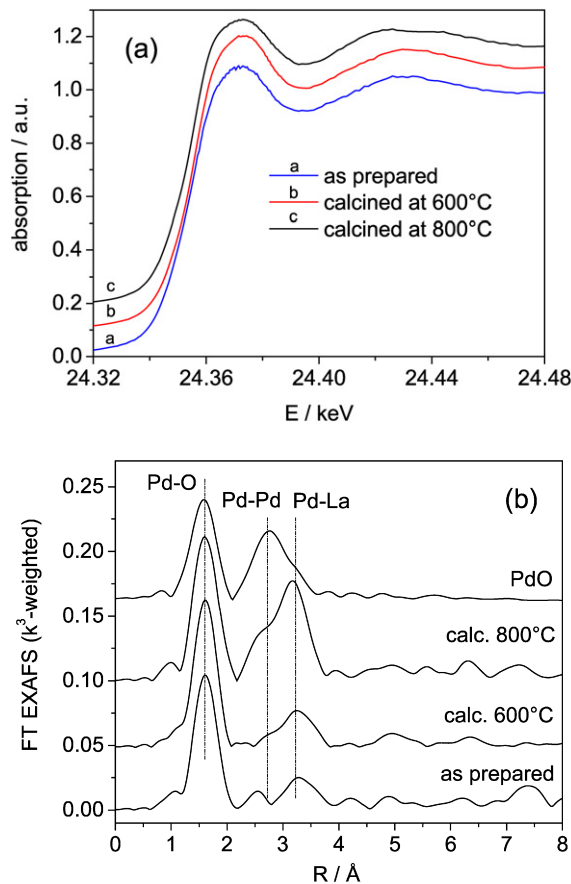


Fig. 4. XANES fluorescence spectra (a) and Fourier transformed k^3 -weighted EXAFS spectra (b) taken in the fluorescence mode at the Pd K-edge of the as-prepared PdLCO and after calcination at 600 and 800 °C.

that no evidence of the presence of Pd in oxidation state +4 was found in the EXAFS spectra at the Pd K-edge; however, the Fourier-transformed EXAFS spectra of the as-prepared samples and the samples calcined at 600 °C differ greatly from those of pure PdO or of PdO supported on ZrO₂ [45,55]. This is due to the absence of a second shell at ca. 2.6 Å, typical of the Pd–Pd distance in PdO (see the reference spectrum of pure PdO in Fig. 4b) and the slightly shorter Pd–O distance compared with that in PdO. This demonstrates that Pd was very finely dispersed in the as-prepared FP-made material. Moreover, the FP-made samples exhibited a contribution at 3.2 Å whose intensity increased with increasing calcination temperature, accompanied by a slight contraction of the Pd–O distance (Table 1, entries 1 to 3). Calculations of theoretical EXAFS spectra using the FEFF code predicted a similar contribution due to the Pd–La bond distance. This important result demonstrates that Pd incorporates into the ABO₃ perovskite lattice at the B site and that the degree of incorporation increases with increasing temperature [56]. In contrast, FT-EXAFS of the sample calcined at 800 °C showed a change in the Pd–Pd and Pd–La environments; in particular, besides the intense Pd–La contribution at 3.2 Å, a shoulder appeared more markedly at 2.7 Å, due to the Pd–Pd distance in palladium-based species (very likely PdO, although we cannot completely exclude the presence of some metallic Pd). This change might indicate a partial segregation of

Table 1
Fit of the EXAFS data at the Pd K-edge^a

Entry	Sample	Shell	CN	<i>R</i> (Å)	σ^2 (Å ²)	ΔE_0 (eV)	Residual (%)
1	As-prepared PdLCO	Pd–O	5.3	2.013	0.0026	11.9	2.5
2	PdLCO, calcined 600 °C	Pd–O	5.6	2.008	0.0025	12.0	4.0
3	PdLCO, calcined 800 °C	Pd–O	6.3	2.008	0.0031	11.2	8.9
4	impPdLCO, reduced 300 °C	Pd–Pd	8.1	2.73	0.0069	1.8	8.1
5	PdLCO, calcined 800 °C, reduced 300 °C	Pd–Pd	6.9	2.73	0.0061	1.8	2.8
6a	PdLCO, calcined 800 °C, reduced 600 °C	Pd–Pd	6.4	2.68	0.0069	12.0	13
6b	PdLCO, calcined 800 °C, reduced 600 °C	Pd–Pd	7.5	2.70	0.0074	2.3	3.7
		Pd–Co	4.3	2.70	0.0074	6.3	

^a CN: coordination number; *R*: interatomic distance; σ^2 : Debye–Waller factor; ΔE_0 : energy shift.

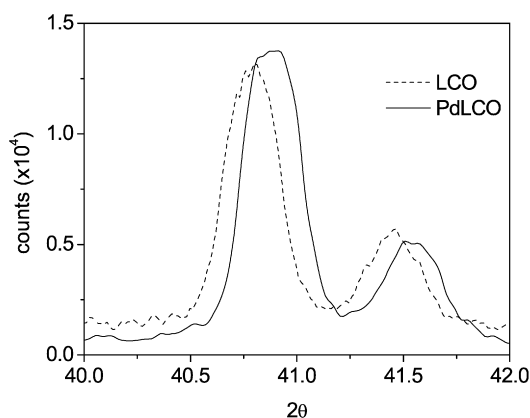


Fig. 5. Room temperature XRD of LCO and PdLCO after calcination at 800 °C.

metallic Pd particles, which reoxidize on cooling in an oxygen-rich atmosphere [57]. Similarly, in a previous investigation on FP-made Pd/Al₂O₃, Strobel et al. reported that during calcination up to 1000 °C, PdO-particles sintered and decomposed to metallic Pd at $T > 800$ °C, but reoxidized back to PdO during cooling at $T < 600$ °C [38].

Regardless, after calcination of PdLCO at 800 °C, Pd was still predominately oxidized and within the perovskite lattice, as confirmed by the comparison of the XRD patterns of PdLCO and LCO after calcination at 800 °C (Fig. 5). A slight shift of the reflections to higher θ values can be observed for PdLCO, due to distortion of the elementary crystal cell caused by the insertion of Pd.

3.2. Reduction of LCO

The TGA profile (Fig. 6a) shows that the reduction of LCO occurred in three steps, as reported in Table 2. Reduction of LaCoO₃ is well documented in the literature. *In situ* XRD during reduction (see Fig. S1 in the supplementary material), similar to those obtained by us, were recently reported for a sol–gel (SG)-made LaCoO₃ [11]. The SG sample reduced in three steps, through “undetectable cobalt species” or, alternatively, through the intermediate formation of La₂CoO₄, which, however, was not clearly assigned in the diffractograms. Indeed, the reduction of LaCoO₃ through the intermediate phases of the general formula La_{*m*+1}Co_{*m*}O_{3*m*+1} anticipates an irreversible decomposition of the perovskite into La₂CoO₄ ($m = 1$)

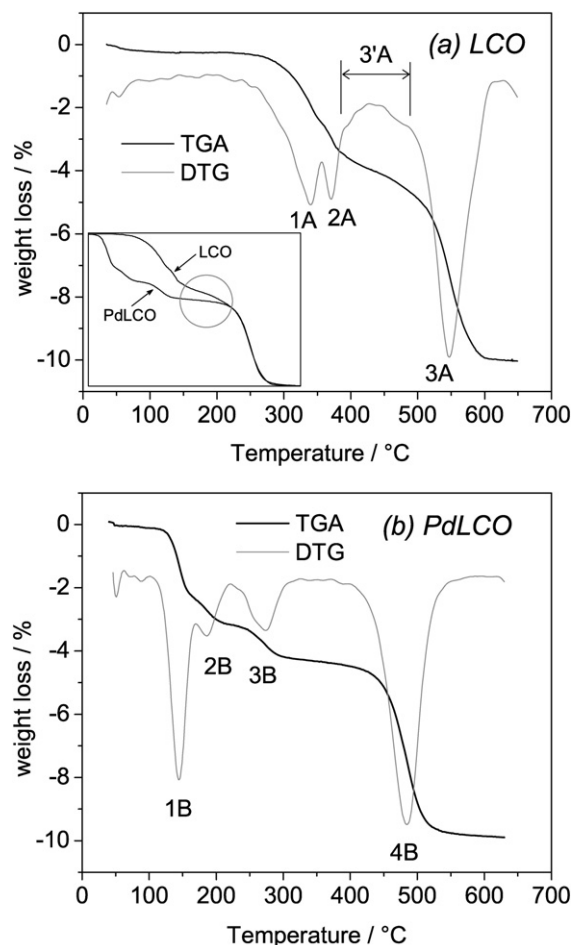


Fig. 6. Thermogravimetric analysis data (TGA, black line) and relative first derivative (DTG, grey line) for reduction in 10% H₂/He of LCO (a) and PdLCO (b). Heating rate 5 °C/min. Inset: horizontal translation and overlapping of the two TGA curves of (a) and (b).

and CoO. Such a pathway has been reported only for reduction processes of LaCoO₃ at high temperature ($T > 600$ °C) [58]. In contrast, the reduction to metallic Co and La₂O₃ at low temperature ($T < 600$ °C) typically occurs through intermediates with nominal composition LaCoO_{3- δ} [21]. In particular, two different intermediate phases of the homologous series La_{*n*}Co_{*n*}O_{3*n*-1} were identified: La₃Co₃O₈ ($n = 3$, $\delta = 0.33$) and La₂Co₂O₅ (brownmillerite type, $n = 2$, $\delta = 0.5$), in which the crystal structure retains the perovskite-type arrangement of

Table 2
Assignment of the processes occurring during the TGA-reduction of LCO preannealed at 800 °C (Fig. 6a)

Step	<i>T</i>	Assignment ^a	XRD phase	t.w.l.	e.w.l.
1A	350 °C	$\text{LaCoO}_3 + (1/3)\text{H}_2 \rightarrow \text{LaCoO}_{2.67} + (1/3)\text{H}_2\text{O}$	$\text{La}_3\text{Co}_3\text{O}_8$	–2.2%	–2.2%
2A	400 °C	$\text{LaCoO}_{2.67} + (1/6)\text{H}_2 \rightarrow \text{LaCoO}_{2.5} + (1/6)\text{H}_2\text{O}$	$\text{La}_2\text{Co}_2\text{O}_5$	–1.1%	–1.1%
3A	550 °C	$\text{LaCoO}_{2.5} + \text{H}_2 \rightarrow (1/2)\text{La}_2\text{O}_3 + \text{Co} + \text{H}_2\text{O}$	$\text{La}_2\text{O}_3 + \text{Co}$	–6.5%	–6.5%
Overall step		$\text{LaCoO}_3 + (3/2)\text{H}_2 \rightarrow (1/2)\text{La}_2\text{O}_3 + \text{Co} + (3/2)\text{H}_2\text{O}$		–9.8%	–9.8%

^a The assignment was made on the basis of the crystal phases detected by *in situ* XRD at the same temperature and by comparing theoretical (t.w.l.) and experimental (e.w.l.) wt% losses.

Table 3
Assignment of the processes observed during the TGA-reduction of PdLCO preannealed at 800 °C (Fig. 6b)

Step	<i>T</i> _{onset}	<i>T</i> _{max}	<i>T</i> _{offset}	e.w.l.	Assignment ^a
1B	100 °C	144 °C	165 °C	–2.2%	$\text{LaCo(Pd)O}_3 \rightarrow \text{La}_3\text{Co(Pd)}_3\text{O}_8$ $\text{PdO} \rightarrow \text{Pd}^0$ $\text{Co}_3\text{O}_4 \rightarrow \text{CoO}$
2B	165 °C	186 °C	220 °C	–0.9%	$\text{CoO} \rightarrow \text{Co}^0$
3B	220 °C	273 °C	330 °C	–1.1%	$\text{La}_3\text{Co(Pd)}_3\text{O}_8 \rightarrow \text{La}_2\text{Co}_2\text{O}_5 + \text{Pd}^0$
4B	390 °C	484 °C	580 °C	–5.6%	$\text{La}_2\text{Co}_2\text{O}_5 \rightarrow \text{La}_2\text{O}_3 + \text{Co}^0$

^a The assignment was made on the basis of the *in situ* XANES and XRD results reported in Figs. 7 and 8, respectively.

the cations. Therefore, $\text{LaCoO}_{3-\delta}$ is generally composed of LaCoO_3 and $\text{La}_3\text{Co}_3\text{O}_8$ for $0.00 < \delta < 0.33$ and of $\text{La}_2\text{Co}_2\text{O}_5$ and $\text{La}_3\text{Co}_3\text{O}_8$ for $0.33 < \delta < 0.50$. These partially reduced structures are thermodynamically unstable with respect to LaCoO_3 and are easily reoxidized after exposure to an oxygen-containing atmosphere at relatively low temperature, but above room temperature [58]. The reoxidation is also facilitated by the relatively open crystal structure, in which the oxygen transport within the matrix is facilitated. In contrast, the full reduction to metallic cobalt and La_2O_3 is irreversible, at least at $T < 500$ °C, with Co being reoxidized to CoO and not back to the perovskite already at room temperature after prolonged exposure to air, as confirmed by *ex situ* XRD measurements (not reported).

Crystal-phase transformations occurring during the reduction process of LCO, monitored by *in situ* XRD (see supplementary material), showed that the LaCoO_3 phase was stable up to 280 °C, whereas its complete reduction occurred at 550 °C, in full agreement with the TGA curve shown in Fig. 6a. Note that the experimental weight loss given in Table 2 is in good agreement with the theoretical weight loss referred to the suggested transformations. This indicates that calcination at 800 °C is likely sufficient to saturate all of the oxygen vacancies of LCO, because the weight loss is due solely to loss of oxygen.

3.3. Reduction of PdLCO

Two species of Pd were observed at this point in PdLCO calcined at 800 °C: segregated PdO particles and Pd^{2+} cations inserted at the B site of the perovskite. The H_2 -TGA-TPR curve of the FP-made PdLCO preannealed at 800 °C (Fig. 6b) showed that in the 50–650 °C temperature range, the reduction proceeded in four steps, which are better resolved in the first-derivative curve. The assignment of the phase transformations responsible for the weight loss was made on the basis of the *in situ* XANES and XRD data (Table 3). The TGA curves of LCO and PdLCO clearly indicate that the presence of Pd

dramatically affected the stability of PdLCO under hydrogen and lowered the temperature of reduction. This process occurred through an additional step—the reduction of Pd^{2+} to metallic Pd—besides the reduction of Co^{3+} to metallic Co. Furthermore, two distinct reduction phenomena occurred, one involving the bulk (i.e., the Pd-doped perovskite) and the other involving the surface (i.e., the surface PdO and Co_3O_4 species). The lattice reduction began at 100 °C, in parallel to the reduction of the surface PdO particles to metallic Pd. The formation of metallic clusters likely triggered the dissociative adsorption of H_2 , leading to the more active H adatoms. This would explain why this material was reduced at lower temperature, as has been observed for other Pd-containing materials [59]. Furthermore, the formation of the $\text{La}_3\text{Co}_3\text{O}_8$ phase was probably thermodynamically favored by the insertion at the B sites of the framework Pd^{2+} . Indeed, Pd^{2+} ions are better accommodated in this structure, where two out of three B sites are occupied by bivalent cations ($\text{B}^{2+}/\text{B}^{3+}$ ratio = 2).

The *in situ* XRD patterns collected during reduction to 700 °C, presented in Fig. 7, closely match the TGA-TPR profile of Fig. 6b. The LaCoO_3 phase was stable up to 100 °C. The diffractogram recorded at 150 °C showed the formation of $\text{La}_3\text{Co}_3\text{O}_8$ ($\text{Co}^{\text{II}}/\text{Co}^{\text{III}}$ ratio = 2) [21]. The reflections relative to this phase became better defined at 200 °C, whereas the Co_3O_4 peak at $2\theta = 36.9^\circ$ disappeared, replaced by a reflection at $2\theta = 42.5^\circ$, attributed to CoO. The formation of $\text{La}_2\text{Co}_2\text{O}_5$ [21] occurred at 300 °C, along with the reduction of CoO to metallic Co particles on the surface ($2\theta = 44.2^\circ$), which also were detected by STEM and whose size can be estimated between 25 and 50 nm (see supplementary material). Finally, the reduction of the whole bulk Co^{2+} to metallic Co occurred at 550 °C. In particular, the pattern recorded at 550 °C showed two La_2O_3 phases: trigonal, in a hexagonal coordinate system, and cubic. The latter appeared already in the diffractogram recorded at 500 °C and disappeared at 700 °C. Moreover, a very intense and typical [54] ferromagnetic signal spectrum of the

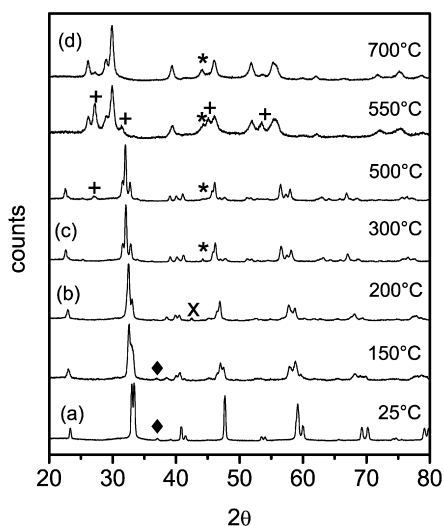


Fig. 7. Normalized *in situ* XRD of PdLCO, precalcined at 800 °C, during reduction in 5% H₂/He at different temperatures up to 700 °C. Patterns attribution: (a) LaCoO₃; (b) La₃Co₃O₈; (c) La₂Co₂O₅; (d) trigonal, in hexagonal coordinate system La₂O₃ and Co phases. The main peaks of the following phases: (◆) Co₃O₄; (×) CoO; (+) cubic La₂O₃; (*) metallic Co; are indicated.

Co nanoparticles was detected by EPR analysis on PdLCO calcined at 800 °C and reduced at 600 °C (Fig. 3d). The size of these nanoparticles can be estimated by HRTEM as on the order of 1 nm (see supplementary material).

Comparison of the two TGA curves of LCO and PdLCO (inset of Fig. 6a) reveals an interesting feature. The third step of LCO reduction (Co²⁺ to Co⁰) occurred through an initial small weight loss in the 390–490 °C range (labelled as 3'A in Fig. 6a), followed by a rapid drop. This suggests that the reduction process involves first the more accessible Co cations of the outer atomic layers, and that it extends to the whole particle only at sufficiently high temperatures. In the case of PdLCO, the former weight loss was absent, because the Co cations involved were already reduced at $T < 300$ °C (step 2B). Therefore, this region appeared flat (the circled zone in the inset of Fig. 6a). In fact, the sum of the weight losses of steps 2B (−0.9%) and 4B (−5.6%) is −6.5%, equal to the weight loss of step 3A. However, the major loss (step 4B) was identical to that of LCO, but shifted to lower temperature. Therefore, the weight loss of step 2B allows for quantification of the amount of Co in the Co₃O₄ phase and thus the amount of surface metallic Co forming after reduction at 300 °C. Indeed, representing the weight loss due to the reaction $\text{CoO} + \text{H}_2 \rightarrow \text{Co} + \text{H}_2\text{O}$, the oxygen atoms leaving the solid as H₂O were in 1:1 molar ratio with respect to the Co²⁺ ions. The amount thus calculated corresponds to 14% of the overall Co or, in other words, 3.5 wt% of the material. Such a high value suggests that the Co atoms involved in formation of the Co₃O₄ phase were not only those segregated from the matrix after substitution by Pd²⁺, but also those present in the external layer and at the edge positions. Their mobility is favored by the high calcination temperature (800 °C), for example, through surface decomposition involving the segregated metallic Pd particles:

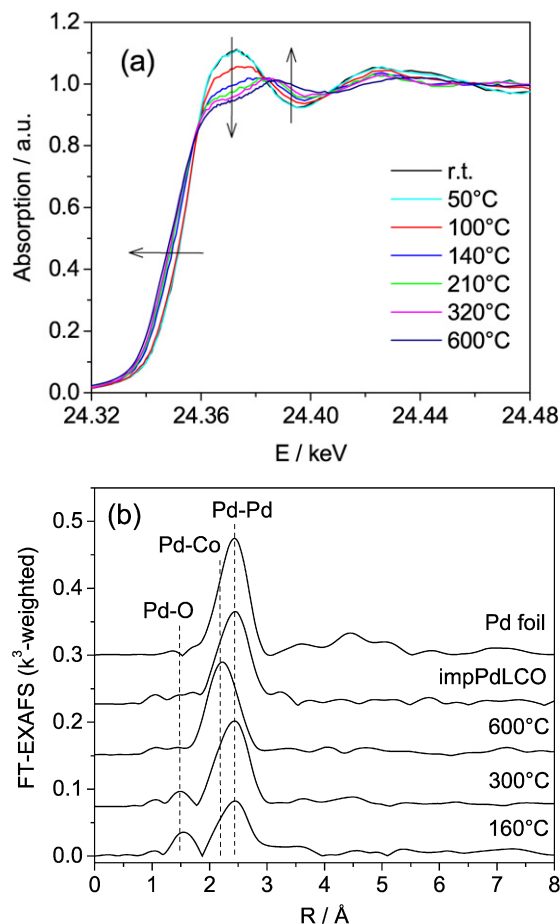


Fig. 8. *In situ* fluorescence XANES spectra at the Pd K-edge (a) and selected Fourier-transformed EXAFS spectra (b) of PdLCO preannealed at 800 °C during reduction in flowing 5% H₂/He at different T up to 600 °C. The arrows indicate the shift with increasing temperature.

Indeed, a shoulder can be observed in the diffractogram of PdLCO calcined at 800 °C at ca. $2\theta = 31^\circ$, where the main reflection of the La₂CoO₄ phase dropped (Fig. 1). The peak appears broad, because few lattice planes contributed to the diffraction. However, it is noteworthy that XRD detected the presence of diffuse scattering due to structural defects, typical of FP-made materials. These defects may make these very active catalysts in oxidation reactions (e.g., the flameless combustion of hydrocarbons), because they facilitate oxygen mobility within the matrix.

The transformations observed during reduction of PdLCO were also followed by *in situ* XANES and EXAFS. The XANES and the Fourier-transformed EXAFS data at selected temperatures are reported in Fig. 8. The XANES spectra confirm that Pd reduction occurred in two steps: at 100 °C for a first fraction of Pd (e.g., PdO particles), and at above 140 °C for the Pd ions incorporated into the perovskite lattice. Complete Pd reduction was achieved at ca. 550 °C, that is, after the loss of the perovskitic structure (compare with Fig. 6a). Fig. 8a shows a clear change in the near-edge structure with increasing temperature, similar to that reported previously for Pd–Co/SiO₂ [60] (but different from that reported for Pd/ZrO₂ [45,55]), indicating a change in the electronic structure due to the progressive

formation of a Pd–Co alloy. The Fourier-transformed EXAFS data show that, compared with the theoretical Pd–Pd distance in Pd foil, the Pd–Pd distance shifted to lower R values with increasing reduction temperature. This shift was not observed in the impPdLCO sample reduced at 300 °C (Fig. 8; Table 1). The Pd–Pd distance in PdLCO contracted from 2.75 Å to a lower value than expected in small noble metal nanoparticles. In all cases, the coordination number was relatively small (<12, with 12 the value for bulk Pd metal), demonstrating that the particle size was rather small (ca. 30 Å). Moreover, the average coordination number (CN) of Pd was smaller in PdLCO than in impPdLCO (entry 4). Thus, more surface atoms were present in PdLCO, and hence the particle size was smaller, resulting in a greater Pd dispersion. PdLCO reduced at 600 °C exhibited a significantly shorter Pd–Pd distance (entry 6) that can be reasonably fitted only by assuming that Pd and Co are neighbors in the first shell of a Pd–Co alloy. In fact, with this approach, the residual error was only 3.7%, compared with 13% when formation of the alloy is neglected. The CN of Pd in the alloy (entry 6b), assuming dodecahedral coordination, revealed that the Pd central atom has an average of 7 Pd atoms and 5 Co atoms around it. Moreover, the total CN of 11.8 ± 1 indicates a considerably larger particle size with respect to the Pd particles in PdLCO prerduced at 300 °C. The surface segregation of Pd, principally as small particles (<10 nm), in FP-made PdLCO after the reduction process has been confirmed by STEM-EDX investigations as well (see supplementary material).

It is worth mentioning that a comparison of the TPR profile of the Pd/LaCoO₃ sample obtained by impregnation of a SG-made LaCoO₃ [11] with that of the FP-made PdLCO identified two major differences: (i) The reduction process of the SG sample occurred in three steps instead of four, and (ii) the first two steps were rather broad and consecutive in the 100–400 °C range, whereas the overall reduction was completed at ca. 600 °C instead of 500 °C. The missing reduction step in the SG sample was likely due to the absence of the Co₃O₄ phase, thus confirming that its formation is strictly related to the presence of Pd in the perovskite lattice. The lattice Pd generated an excess of B-type cations, with the consequent segregation of Co. However, the presence of Pd in the lattice made the perovskite more accessible to reducing agents, so that it reduced at lower temperatures.

3.4. Stability of reduced PdLCO in O₂-rich atmosphere

In the previous sections, we showed that reduction of PdLCO at 300 °C produced Pd/Co/La₂Co₂O₅. This phase was thermodynamically metastable, and it reoxidized to Pd/Co/La₃Co₃O₈ after overnight exposure to air at room temperature (Fig. 9c). Furthermore, *in situ* XRD experiments (Fig. 9b) showed that Pd/Co/La₂Co₂O₅ oxidized to Pd/Co/LaCoO₃ in flowing 21% O₂/He at 160 °C. In particular, no reflections of Co₃O₄ or CoO were detected at this temperature. A weak peak of the Co₃O₄ crystal phase at $2\theta = 36.9^\circ$ could be seen only on the XRD pattern recorded at 250 °C, indicating that the bulk reoxidation of the segregated Co particles occurred at $T > 160^\circ\text{C}$. However, we cannot exclude the possibility that

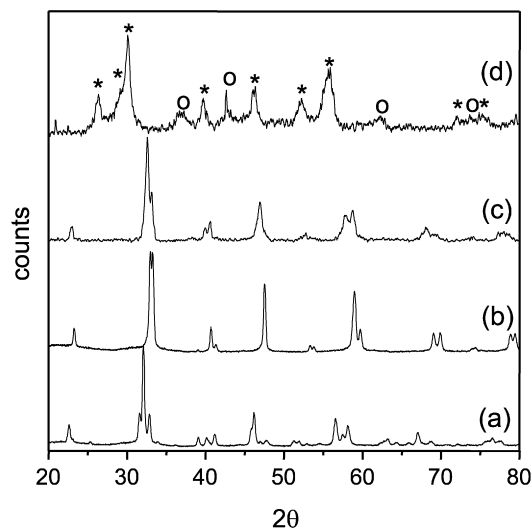


Fig. 9. Normalized XRD of PdLCO: (a) calcined at 800 °C and reduced at 300 °C; (b) calcined at 800 °C, reduced at 300 °C and reoxidized at 160 °C in flowing 21% O₂/He; (c) calcined at 800 °C, reduced at 300 °C and exposed overnight to air at r.t.; (d) calcined at 800 °C, reduced at 600 °C and exposed overnight to air at r.t. Phase attribution: (a) La₂Co₂O₅; (b) LaCoO₃; (c) La₃Co₃O₈; (d) La₂O₃ (*); and CoO (○).

surface oxidation of these particles might have occurred already at lower temperatures [12]. The temperature of 160 °C was chosen because it is the temperature at which the maximum NO conversion is reached in the NO/H₂/O₂ reaction for perovskite-supported noble metals [9–13]. Importantly, XANES spectra indicated that Pd remains in the metallic state after reoxidation of the perovskite at 160 °C. Thus, the final composition of the material obtained after calcination at 800 °C, reduction at 300 °C, and reoxidation at 160 °C can be written as 0.5 wt% Pd/3.5 wt% Co/LaCo_{1-x}O_{3-δ}. This formulation indicates that, unlike the traditional material, the FP-prepared material exhibited surface metallic Co along with Pd particles. Because Pd strongly affects Co reducibility (*vide supra*), this may anticipate a possible synergy between Pd and Co nanoparticles and the perovskite support in catalytic processes involved in the control of exhaust emissions. Furthermore, the selective catalytic reduction of NO (SCR) can proceed efficiently with Co/SiO₂ and Co/Al₂O₃ if Co is well dispersed on the support surface [61,62].

On the other hand, PdLCO reduced at 600 °C produced a Pd–Co/Co/La₂O₃ mixed phase. After overnight exposure to air at room temperature or at 160 °C, this material oxidized to Pd–Co/CoO–La₂O₃ (Fig. 9d), and no significant change occurred in the XANES and EXAFS spectra. These findings indicate that the Pd–Co alloy was more stable to reoxidation than the dispersed Co particles alone.

It is noteworthy that the different oxidizability of the Co particles forming from reduction of the perovskite support with size on the order of 1 nm compared with the greater than one order of magnitude larger segregated Co particles is closely connected to the size difference. Indeed, it is well known that the smaller their size, the more readily these particles oxidize.

Finally, it should be mentioned that the formation of a Pd–Co alloy is reputedly detrimental, because the lower melting point of the alloy compared with that of metallic Pd promotes

particle growth at high temperature, with a consequent loss in catalytic activity [63]. However, we found that the Pd–Co alloy was more active than metallic Pd in the low-temperature (ca. 160 °C) NO/H₂/O₂ reaction [44].

4. Conclusion

The main result of the present investigation is that some properly selected activation thermal treatments allow one to tune-up the structure of the FP-prepared Pd–LaCoO₃-system. The one-step FP synthetic route produced a pure perovskite-like material doped with the precious metal, entering into the B site of the perovskite lattice as Pd²⁺. This material exhibited significantly different properties than the sample prepared by impregnation, with a high surface area and structural defects, making it interesting for catalytic applications. The material was stable under oxidizing conditions up to 600 °C, whereas at 800 °C, partial segregation of Co₃O₄ and Pd⁰ occurred. After calcination at 800 °C, Pd was found both within the perovskite lattice and as segregated PdO. Reduction at 300 °C of the sample calcined at 800 °C resulted in metallic Pd and Co particles on the LaCoO_{3–δ} crystals. Simultaneously, the perovskite transformed into a series of intermediate phases that still exhibited a perovskite-like structure. Mild reoxidation at 160 °C regenerated the LaCoO₃ perovskite support and left Pd in the reduced state. In contrast, reduction at 600 °C followed by exposure to air generated a Pd–Co alloy supported on CoO–La₂O₃.

Acknowledgments

The authors thank the Hamburger Synchrotronstrahlungslabor (HASYLAB) at the Deutsches Elektronen-Synchrotron for providing beamtime for the *in situ* XRD studies, and the Swiss–Norwegian beamline at ESRF for providing *in situ* EXAFS measurements in the fluorescence mode. They also thank C. Baecht at HASYLAB and H. Emmerick and W. van Beek at ESRF are acknowledged for their kind support during the experiments, and Dr. M. Maciejewski for the TGA measurements and fruitful discussions. G.L.C. is grateful for a scholarship from the University of Milano.

Supplementary material

The online version of this article contains additional supplementary material.

Please visit DOI: [10.1016/j.jcat.2007.10.004](https://doi.org/10.1016/j.jcat.2007.10.004).

References

- [1] H.U. Blaser, A. Indolese, A. Schnyder, H. Steiner, M. Studer, J. Mol. Catal. A Chem. 173 (2001) 3.
- [2] G. Centi, J. Mol. Catal. A Chem. 173 (2001) 287.
- [3] D. Ciuparu, M.R. Lyubovsky, E. Altman, L.D. Pfefferle, A. Datye, Catal. Rev.-Sci. Eng. 44 (2002) 593.
- [4] P. Gelin, M. Primet, Appl. Catal. B Environ. 39 (2002) 1.
- [5] R.M. Heck, R. Farrauto, S.T. Gulati, Catalytic Air Pollution Control, second ed., Wiley–Interscience, New York, 2002.
- [6] M.A. Pena, J.L.G. Fierro, Chem. Rev. 101 (2001) 1981.
- [7] S. Cimino, L. Lisi, G. Russo, Ind. Eng. Chem. Res. 43 (2004) 6670.
- [8] R. Zhang, A. Villanueva, H. Alamdari, S. Kaliaguine, J. Catal. 237 (2006) 368.
- [9] C.N. Costa, V.N. Stathopoulos, V.C. Belessi, A.M. Efstathiou, J. Catal. 197 (2001) 350.
- [10] C.N. Costa, P.G. Savva, C. Andronikou, P.S. Lambrou, K. Polychronopoulou, V.C. Belessi, V.N. Stathopoulos, P.J. Pomonis, A.M. Efstathiou, J. Catal. 209 (2002) 456.
- [11] M. Engelmann-Pirez, P. Granger, G. Leclercq, Catal. Today 107–108 (2005) 315.
- [12] I. Twagirashema, M. Engelmann-Pirez, M. Frere, L. Burylo, L. Gengembre, C. Dujardin, P. Granger, Catal. Today 119 (2007) 100.
- [13] C.N. Costa, A.M. Efstathiou, J. Phys. Chem. B 108 (2004) 2620.
- [14] S. Petrovic, L. Karanovic, P.K. Stefanov, M. Zdujic, A. Terlecki-Baricevic, Appl. Catal. B Environ. 58 (2005) 133.
- [15] M.J. Koponen, T. Venäläinen, M. Suvanto, K. Kallinen, T.J.J. Kinnunen, M. Härkönen, T.A. Pakkanen, Appl. Catal. A Gen. 311 (2006) 79.
- [16] S. Specchia, A. Civera, G. Saracco, V. Specchia, Catal. Today 117 (2006) 427.
- [17] Y. Nishihata, J. Mizuki, T. Akao, H. Tanaka, M. Uenishi, M. Kimura, T. Okamoto, N. Hamada, Nature 418 (2002) 164.
- [18] M. Uenishi, M. Taniguchi, H. Tanaka, M. Kimura, Y. Nishihata, J. Mizuki, T. Kobayashi, Appl. Catal. B Environ. 57 (2005) 267.
- [19] H. Tanaka, Catal. Surv. Asia 9 (2005) 63.
- [20] T. Nakamura, G. Petzow, L.J. Gauckler, Mater. Res. Bull. 14 (1979) 649.
- [21] O.H. Hansteen, H. Fjellvag, B.C. Hauback, J. Mater. Chem. 8 (1998) 2081.
- [22] L. Huang, M. Bassir, S. Kaliaguine, Appl. Surf. Sci. 243 (2005) 360.
- [23] S. Cimino, G. Landi, L. Lisi, G. Russo, Catal. Today 117 (2006) 454.
- [24] T. Johannessen, J.R. Jensen, M. Mosleh, J. Johansen, U. Quadde, H. Livbjerg, Chem. Eng. Res. Des. 82 (2004) 1444.
- [25] R. Strobel, A. Baiker, S.E. Pratsinis, Adv. Powder Technol. 17 (2006) 457.
- [26] T. Johannessen, S. Koutsopoulos, J. Catal. 205 (2002) 404.
- [27] J.R. Jensen, T. Johannessen, S. Wedel, H. Livbjerg, J. Catal. 218 (2003) 67.
- [28] R. Strobel, F. Krumeich, W.J. Stark, S.E. Pratsinis, A. Baiker, J. Catal. 222 (2004) 307.
- [29] L. Fabbrini, A. Kryukov, S. Cappelli, G.L. Chiarello, I. Rossetti, C. Oliva, L. Forni, J. Catal. 232 (2005) 247.
- [30] R. Strobel, L. Maedler, D. Beydoun, M. Maciejewski, A. Baiker, S.E. Pratsinis, Chem. Mater. 18 (2006) 2532.
- [31] W.Y. Teoh, L. Maedler, D. Beydoun, S.E. Pratsinis, R. Amal, Chem. Eng. Sci. 60 (2005) 5852.
- [32] R. Strobel, S.E. Pratsinis, A. Baiker, J. Mater. Chem. 15 (2005) 605.
- [33] R. Strobel, W.J. Stark, L. Mädler, S.E. Pratsinis, A. Baiker, J. Catal. 213 (2003) 296.
- [34] J.R. Jensen, T. Johannessen, S. Wedel, H. Livbjerg, J. Catal. 218 (2003) 67.
- [35] R. Strobel, L. Madler, M. Piacentini, M. Maciejewski, A. Baiker, S.E. Pratsinis, Chem. Mater. 18 (2006) 2532.
- [36] S. Koutsopoulos, T. Johannessen, K.M. Eriksen, R. Fehrmann, J. Catal. 238 (2006) 206.
- [37] N. van Vegten, D. Ferri, M. Maciejewski, F. Krumeich, A. Baiker, J. Catal. 249 (2007) 269.
- [38] R. Strobel, J.D. Grunwaldt, A. Camenzind, S.E. Pratsinis, A. Baiker, Catal. Lett. 104 (2005) 9.
- [39] S. Hannemann, J.D. Grunwaldt, F. Krumeich, P. Kappen, A. Baiker, Appl. Surf. Sci. 252 (2006) 7862.
- [40] S. Hannemann, J.D. Grunwaldt, P. Lienemann, D. Günther, F. Krumeich, A. Baiker, Appl. Catal. A Gen. 316 (2007) 226.
- [41] G.L. Chiarello, I. Rossetti, L. Forni, J. Catal. 236 (2005) 251.
- [42] G.L. Chiarello, I. Rossetti, P. Lopinto, G. Migliavacca, L. Forni, Catal. Today 117 (2006) 549.
- [43] G.L. Chiarello, I. Rossetti, L. Forni, P. Lopinto, G. Migliavacca, Appl. Catal. B Environ. 72 (2007) 218.
- [44] G.L. Chiarello, J.D. Grunwaldt, D. Ferri, A. Baiker, L. Forni, J. Catal. 252 (2007) 137.
- [45] J.D. Grunwaldt, M. Caravati, S. Hannemann, A. Baiker, Phys. Chem. Chem. Phys. 6 (2004) 3037.
- [46] T.J. Ressler, Syn. Rad. 5 (1998) 118.

- [47] S.I. Zabinsky, J.J. Rehr, A. Ankudinov, R.C. Albers, M.J. Eller, *Phys. Rev. B* 52 (1995) 2995.
- [48] M. Maciejewski, W.D. Emmerich, A. Baiker, *J. Therm. Anal. Calorim.* 56 (1999) 627.
- [49] C. Oliva, S. Cappelli, A. Kryukov, G.L. Chiarello, A.V. Vishniakov, L. Forni, *J. Mol. Catal. A Chem.* 255 (2006) 36.
- [50] A.S. Sass, V.A. Shvets, G.A. Savel'eva, N.M. Popova, V.N. Kazansky, *Kinet. Katal.* 24 (1983) 1167.
- [51] A. Fresauld, S. Khairoun, J.M. Dance, P. Hagemuller, *Z. Anorg. Allg. Chem.* 517 (1984) 43.
- [52] B.A. Goodman, J.B. Raynor, *Adv. Inorg. Chem.* 13 (1970) 304.
- [53] I.N. Filimonov, I.A. Ikonnikov, A.Y. Loginov, *J. Chem. Soc. Faraday Trans.* 90 (1994) 219.
- [54] S.P. Gubin, Y.I. Spichkin, Y.A. Koksharov, G.Y. Yurkov, A.V. Kozinkin, T.I. Nedoseikina, M.S. Korobov, A.M. Tishin, *J. Magn. Magn. Mater.* 265 (2003) 234.
- [55] J.D. Grunwaldt, M. Maciejewski, A. Baiker, *Phys. Chem. Chem. Phys.* 5 (2003) 1481.
- [56] S.J. Kim, S. Lemaux, G. Demazeau, J.Y. Kim, J.H. Choy, *J. Mater. Chem.* 12 (2002) 995.
- [57] R.J. Farrauto, J.K. Lampert, M.C. Hobson, E.M. Waterman, *Appl. Catal. B Environ.* 6 (1995) 263.
- [58] M. Seppänen, M. Kitö, P. Taskinen, *Scand. J. Metall.* 8 (1979) 199.
- [59] W.J. Stark, J.D. Grunwaldt, M. Maciejewski, S.E. Pratsinis, A. Baiker, *Chem. Mater.* 17 (2005) 3352.
- [60] L. Gucci, L. Borko, Z. Schay, D. Bazin, *Catal. Today* 65 (2001) 51.
- [61] M. Inaba, Y. Kintaichi, M. Haneda, H. Hamada, *Catal. Lett.* 39 (1996) 269.
- [62] H. Hamada, Y. Kintaichi, M. Inaba, M. Tabata, T. Yoshinari, H. Tsuchida, *Catal. Today* 29 (1996) 53.
- [63] I. Tan, H. Tanaka, M. Uenishi, K. Kaneko, S. Mitachi, *J. Ceram. Soc. Jpn.* 113 (2005) 71.